XMM-Newton view of X-ray overdensities from nearby galaxy clusters: the environmental dependencies

Turgay Caglar,[1]⋆ Murat Hudaverdi,[2,1]

[1]*Department of Physics, Yildiz Technical University, Davutpasa Campus, 34220, Istanbul, Turkey*
[2]*AUM, College of Engineering and Technology, Department of Science, Dasman 15453, Kuwait*

ABSTRACT

In this work, we studied ten nearby (z⩽0.038) galaxy clusters to understand possible interactions between hot plasma and member galaxies. A multi-band source detection was applied to detect point-like structures within the intra-cluster medium. We examined spectral properties of a total of 391 X-ray point sources within cluster's potential well. Log N - Log S was studied in the energy range of 2-10 keV to measure X-ray overdensities. Optical overdensities were also calculated to solve suppression/triggering phenomena for nearby galaxy clusters. Both X-ray to optical flux/luminosity properties, $(X/O, L_X/L_B, L_X/L_K)$, were investigated for optically identified member galaxies. X-ray luminosity values of our point sources are found to be faint $(40.08 \leqslant \log(L_X) \leqslant 42.39 \text{ erg s}^{-1})$. The luminosity range of point sources reveals possible contributions to X-ray emission from LLAGNs, X-ray Binaries and star formation. We estimated ∼ 2 times higher X-ray overdensities from galaxies within galaxy clusters compared to fields. Our results demonstrate that optical overdensities are much higher than X-ray overdensities at the cluster's centre, whereas X-ray overdensities increase through the outskirts of clusters. We conclude that high pressure from the cluster's centre affects the balance of galaxies and they lose a significant amount of their fuels; as a result, clustering process quenches X-ray emission of the member galaxies. We also find evidence that the existence of X-ray bright sources within cluster environment can be explained by two main phenomena: contributions from off-nuclear sources and/or AGN triggering caused by galaxy interactions rather than AGN fuelling.

Key words: galaxies: active – galaxies: clusters: general – X-rays: galaxies – X-rays: galaxies: clusters – galaxies: clusters: intracluster medium – galaxies: clusters: individual

1 INTRODUCTION

Clusters of galaxies are formed by gravitational infalling of smaller structures, and thus they are observed to be in high density regions of the Universe. Their deep potential well retains hot gas and individual galaxies in the vicinity. The morphology and star formation rate (SFR) of such infalling galaxies change as a result of their interaction with the intra-cluster medium (ICM). Possible interactions and collisions between member galaxies are very likely probable. All these complexities can be effective on the galaxy evolution within galaxy clusters. The advents of the technology in space science allow us to study the evolution of galaxies in these dense and complex regions.

Several studies at different redshifts report X-ray source overdensities from galaxy clusters (e.g., Cappi et al. 2001; D'Elia et al. 2004; Hudaverdi et al. 2006; Gilmour et al. 2009; Koulouridis & Plionis 2010; Ehlert et al. 2013). The comparison between clustered and non-clustered fields has been very successful to explain the nature of X-ray point sources. However, it is still unclear whether cluster environments suppress or enhance X-ray active galactic nuclei (AGN) activity. Koulouridis & Plionis (2010) attempted to answer this issue by comparing X-ray and optical overdensities from 16 rich Abell clusters and reported a strong suppression within the dense (< 1 Mpc) cluster environment. Khabiboulline et al. (2014) studied low redshift clusters (z < 0.2) and showed that AGN activity is suppressed in the rich cluster centre. Haines et al. (2012) also confirmed a similar result for massive clusters. On the other hand, radially mov-

⋆ E-mail: turgay.caglar@std.yildiz.edu.tr

ing outward to the cluster outskirts, Ruderman & Ebeling (2005) showed an enhancement of X-ray AGN activity for 51 clusters within 3.5 Mpc. This result is also confirmed for distant clusters ($z > 1$) by further investigations (Fassbender et al. 2012; Koulouridis et al. 2014, 2016; Alberts et al. 2016). A recent study found evidence that AGN emission is found to be strongly related to the richness class of the host cluster. It is understood that rich clusters suppress X-ray AGN activity (e.g., Koulouridis & Plionis 2010; Ehlert et al. 2013; Haines et al. 2012; Koulouridis et al. 2014). On the similar topic, Bufanda (2017) did not, however, find any clear correlation between AGN fraction and cluster richness based on a study of 432 galaxy clusters' data in the redshift range $0.10 < z < 0.95$. Therefore, The role of environment in the frequency of AGN is still an open question. A number of studies demonstrate an increased nuclear activity of the galaxies in the rich cluster environment. Martini et al. (2006) verified the existence of large low-luminous active galactic nuclei (LLAGN) populations and reported the fraction as ~5% in the nearby galaxy clusters. Furthermore, Melnyk et al. (2013) reported that 60% of X-ray selected AGNs are found to be in dense environments and thus likely to reside in clusters of galaxies. Ellison et al. (2011) reported substantial evidence of increased AGN activity due to close encounters of galaxies in the gravitational potential well of the host cluster. Haggard et al. (2010) estimated approximately equal optical AGN fraction from clusters relative to the fields. Ehlert et al. (2013, 2014) found X-ray AGN fraction of 42 massive cluster centres to be three times lower than the fields. Traditional optical studies reveal a lower optical AGN fraction from clusters; the fraction for cluster and non-cluster fields is found to be ~1% and ~5%, respectively (e.g., Dressler et al. 1999). Recent studies also confirm that optically bright AGNs are rare in cluster environments (e.g., Kauffmann et al. 2004; Popesso & Biviano 2006).

The main astrophysical objects responsible for X-ray emission are diffuse hot gas, X-ray Binaries (XRBs) and accreting supermassive black holes (SMBHs); therefore X-ray emission mechanisms are highly related to the dynamic events occurring within the galaxy. In the case of absence of very luminous X-ray sources, galaxy X-ray emission fainter than Lx $< 10^{42}$ erg s^{-1} can be produced either from star formation activities or LLAGNs. Recent studies imply that X-ray emission from the majority of LLAGNs can be related to off-nuclear sources or diffuse emission rather than central nuclear emission (e.g., Ho et al. 2001; Ranalli et al. 2003; Ranalli 2012). On the other hand, Gisler et al. (1978) provided a correlation between star-formation and dense environments: galaxies have low star formation rates in crowd regions. Recent studies also confirmed this relationship (e.g., Kauffmann et al. 2004; Schaefer et al. 2017). Observed low star formation rates from corresponding galaxies are highly relative to the distance from central regions of clusters and associated with environmental suppression (e.g., Oemler 1974; Balogh et al. 1997; Wetzel et al. 2014). To understand properties of the star forming galaxies, some indicators have been derived from multi-wavelength surveys (Ranalli et al. 2003; Mineo et al. 2012).

In this study, we aim to understand the contribution of environment to the galaxy evolution and interaction between ICM and member galaxies. We also intend to measure X-ray and optical density of selected galaxy clusters. There

Table 1. XMM-Newton observation logs of our sample of clusters.

Obj. Name	Obs. ID	Obs. Date	Exp. Time (ks) M1 M2 PN
Abell 3581	0504780301	01/08/2007	117 117 113
Abell 1367	0061740101	26/05/2001	33 33 28
Abell 1314	0149900201	24/11/2003	18 18 17
Abell 400	0404010101	06/08/2006	39 39 33
Abell 1836	0610980201	17/01/2010	37 37 35
Abell 2063	0550360101	23/07/2008	28 28 24
Abell 2877	0204540201	23/11/2004	22 22 20
Abell S137	0744100101	16/05/2014	27 27 32
Abell S758	0603751001	21/02/2010	64 64 60
RXCJ2315.7-0222	0501110101	22/11/2007	44 44 40
Deep 1334+37	0109661001	23/06/2001	86 86 86
Groth-Westphal	0127921001	21/07/2000	56 56 52
Hubble Deep N	0111550301	27/05/2001	46 46 45

is a conflict whether galaxy clustering process suppresses or enhances galaxy X-ray activity. We attempt to solve this conflict in nearby clusters by searching for X-ray and optical overdensities relative to fields. We selected a sample of several nearby galaxy clusters ($\leqslant$ 171 Mpc). However, in bright galaxy clusters, faint X-ray point sources cannot be detected in very bright ICMs. In that case, X-ray source number densities can be decreased. To overcome this effect, we concentrated on faint galaxy clusters with unextended ICM emission ($r_c < 170$ kpc). Our paper is organised as follows: Section 2 reviews observational samples and the data reduction process. Section 3 describes how we performed X-ray and optical analysis. Section 4 describes our measurement method for X-ray and optical overdensities. In section 5, we discuss our results in two different topics: contribution to X-ray emission from LLAGNs and star formation. Section 6 concentrate on the nature of X-ray and optical emission from individual galaxies. Finally, in section 7, we present our conclusions. We adopt WMAP standard cosmological parameters $H_0 = 70$ km s^{-1} Mpc^{-1}, $\Omega_M = 0.27$ and $\Omega_\Lambda = 0.73$ in a flat universe.

2   OBSERVATION AND DATA REDUCTION

We used archival data of the *XMM-Newton* in our analysis, and all observational data were gathered from *XMM-Newton* Science Archive (XSA). In our survey, we concentrated on selecting the *XMM-Newton* observational data that were taken in full frame mode for MOS and extended full frame mode for pn. X-ray observation data logs are listed in Table 1.

The *XMM-Newton* data were processed by using *heasoft 6.19* and *XMMSAS 15.0.0* current calibration files (ccf) and summarised observation data files (odf) were generated by using *cifbuild-4.8* and *odfingest-3.30* respectively. We generated event files using *epchain-8.75.0* and *emchain-11.19* tasks from the observation data file. Rate filter is applied to the event file to clear flaring particle background.

3 ANALYSIS

3.1 Spatial and Spectral Analysis

We applied SAS source detection algorithms to the data. Source detection was performed by using SAS task, namely *edetect_chain-3.14.1*. We used five different images in the super soft band (0.2-0.5 keV), in the soft band (0.5-1.0 keV), in the medium band (1.0-2.0 keV), in the hard band (2.0-4.5 keV), and in the super hard band (4.5-12.0 keV) for source detection. Source detections were accepted with likelihood values above 10 (about 4 σ) and inside an off-axis angle of 12.5′. Detection routine was applied for both mos and pn cameras, and the final list was combined with sas task '*srcmatch-3.18.1*'. After detecting point-like sources, spectral and background files were produced by using sas task *evselect-3.62*. The background spectrum was extracted from an annulus surrounding the circular source region. Area of spectral files was calculated by using *backscale-1.4.2*. The Redistribution Matrix Files and Ancillary Response Files were produced by using SAS tasks *rmfgen-2.2.1* and *arfgen-1.92.0* respectively. The spectra of a majority of the point sources were modelled with a single absorbed power-law. However, the spectra of several sources contain thermal emission lines that cannot be fit well by using a single power law. In that situation, we added a thermal component (APEC) to improve fitting. The average intra-galactic abundance value was fixed at 0.3 solar value in our analysis (Getman et al. 2005).

3.2 Sensitivity of the Survey

The sky coverage represents the survey area of the observed source and decreases with flux due to instrumental effects. Therefore, limiting flux of our survey needs to be calculated very carefully. There are a few factors that affect limiting flux, such as point spread function, vignetting, exposure time, and detector sensitivity. We calculated the sensitivity of our cameras by using sas task *esensmap-3.12.1*. The energy conversion factors of our samples (ECF) were calculated from rate/flux by considering hydrogen column density, photon index, and filter type of operating camera. ECF values of our samples were calculated with XSPEC model (wabs*power) with fixed photon index of 1.7 and fixed total galactic hydrogen column density value. Resulting ECF values and limit flux of our samples are presented in Table 2. Since galaxy clusters emit centrally concentrated very diffuse X-ray emission, the detection of the faint sources buried inside the ICM is not possible. To overcome this problem, we did not take into account the central region of our sample of clusters ($\sim 3 \times r_c$) in our analysis. Central regions of each cluster ($95 < r_c < 145$ h$_{70}^{-1}$ kpc) were calculated from King's Profile (King 1962). Due to these selection techniques, X-ray sources fainter than 1×10^{-14} erg cm^{-2} s^{-1} were not taken into consideration in our analysis, and we also didn't present their properties in the appendix.

3.3 Optical Data

Even though a small number of red spirals and blue ellipticals are reported in the literature (e.g., Van den Bergh 1976; Masters et al. 2010), spiral galaxies are typically found in

Table 2. Detection sensitivity survey: I) Name of the galaxy cluster II) Energy conversion factor III) A total number of detected sources IV) Final source number V) Flux limit of the corresponding cluster.

I Cluster	II ECF cts cm^2 erg^{-1}	III N$_T$	IV N$_F$	V Limit Flux erg cm^{-2} s^{-1}
Abell 1367	4.72×10^{11}	71	33	6.76×10^{-15}
Abell 3581	4.91×10^{11}	105	47	4.07×10^{-15}
Abell 400	3.81×10^{11}	62	33	6.17×10^{-15}
Abell 2877	4.78×10^{11}	69	35	5.50×10^{-15}
Abell S137	5.07×10^{11}	91	54	3.80×10^{-15}
Abell 1314	4.46×10^{11}	111	39	5.25×10^{-15}
Abell 2063	5.21×10^{11}	34	25	7.59×10^{-15}
Abell 1836	4.17×10^{11}	116	32	6.31×10^{-15}
Abell S758	4.58×10^{11}	130	59	2.88×10^{-15}
RXCJ2315.7-0222	4.25×10^{11}	85	34	4.17×10^{-15}

blue clouds, while ellipticals are usually on the red sequence (e.g., Tully et al. 1982; Kauffmann et al. 2003; Tojeiro et al. 2013). The fraction of early-type galaxies with respect to the whole galaxy population is significantly higher in clusters than in the field (e.g., Oemler 1974; Dressler 1980; Dressler et al. 1999; Kauffmann et al. 2004), whereas the number of the blue-type galaxies increases towards the outskirts of the clusters (e.g., Butcher & Oemler 1978; Pimbblet et al. 2002). In this section, we aim to identify the colour of galaxies (blue/red) within cluster fields.

Optical counterparts of X-ray sources are identified from SDSS archive. However, we note that not all X-ray sources have optical counterparts. Also, X-ray centroid of galaxies does not always coincide with optical centroids. It is well known that major events, such as clusters mergers or tidal interactions, cause offset between X-ray and optical centre (e.g., Peres et al. 1998). Loaring et al. (e.g., 2013) demonstrated the existence of a trend between flux and positional error for *XMM-Newton* point sources and reports maximum positional error of *XMM-Newton* for faint sources as $< 10''$ within off-axis angle 9′; moreover, the positional error of sources becomes higher at the off-axis angle $> 9'$. Owing to these assumptions, we considered optical counterpart of X-ray sources within $< 6''$ (< 4.7 kpc) radius. Then, likelihood ratio for each candidate is computed by using cross-correlation method described by Pineau et al. (e.g. 2011, and references therein). Finally, sources falling outside the likelihood ratio $< \%50$ are assumed as background sources. We also mention that similar methods were applied to different surveys (e.g., Brusa et al. 2010; Flesch 2010; Pineau et al. 2011; LaMassa et al. 2013). We exhibit galaxy r band magnitudes as a function of g-r and b-r in Fig. 1. Magnitude values were taken from SDSS archive for the following galaxy clusters: A400, A1314, A1367, A1836, A2063, and RXCJ2315.7-0222. However, there are no SDSS observations for the rest of the galaxy clusters. To study them, we used three different catalogues to gather b and r band magnitudes of galaxies (Flesch 2010; Zacharias et al. 2005, 2013). We also note that the K and extinction correction are applied to all magnitude values unless they are noted as extinction corrected. Dashed lines represent the limit value to separate blue and red galaxies (López-Cruz et al. 2004; Laganá et al. 2009). We identified a control zone using g-
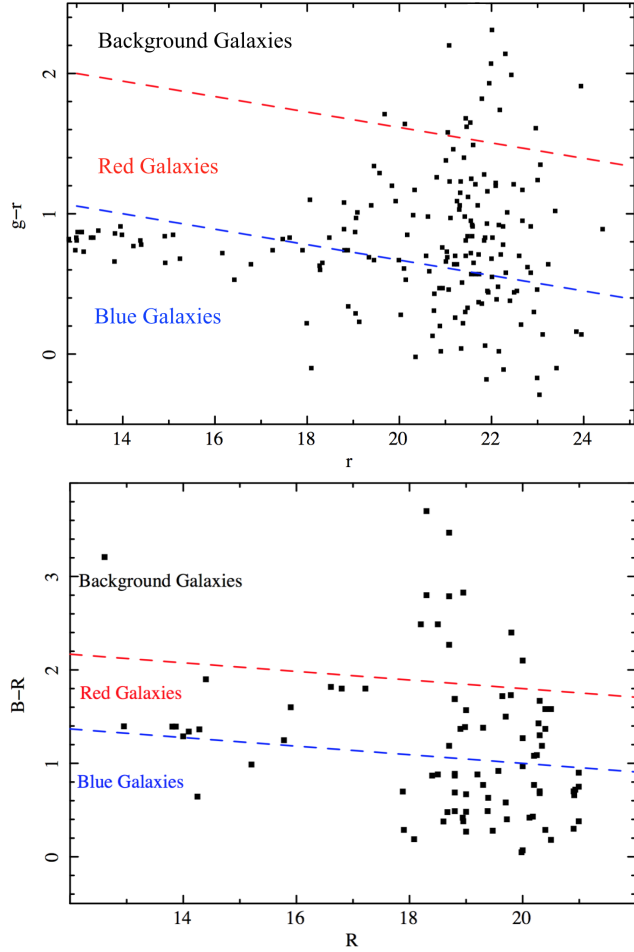
Figure 1. Colour-magnitude diagram of galaxies within our sample of clusters.

r ±0.4 limit for background galaxies. We assume that the galaxies falling outside of upper limit of the red sequence are unrelated to galaxy clusters.

4   OVERDENSITY MEASUREMENTS

The number of sources per unit sky area with the flux higher than S, N (> S), is defined as ;

$$N(>S) = \sum_{i=1}^{n} \frac{1}{\Omega_i} deg^{-2} \qquad (1)$$

where n is number of detected sources, Ω_i is sky coverage for the flux of the i-th source. Fig. 2 shows log N - log S for our samples and their comparison with Lockman hole result, which was calculated by Hasinger et al. (2001). Several studies show that cosmic variance within 2-10 keV energy range is less than 15% (e.g., Cappelluti et al. 2005; Dai et al. 2015); hence, we selected 2-10 keV flux values for our log N - log S measurements. In our survey, sources brighter than log($f_{2-10keV}$) = -13.5 erg cm^{-2} s^{-1} are not affected by decreasing of sky coverage, with this; we calculate X-ray overdensities at this particular flux value. At log($f_{2-10keV}$) = -13.5 erg cm^{-2} s^{-1}, Hasinger et al. (2001) estimated 52±7

Table 3. Our sample of clusters: X-ray overdensities. ★: N(>S) values at log($f_{2-10keV}$) = -13.5 erg cm^{-2} s^{-1}.

Cluster	Redshift	δ_X	$m_r{}^*$ mag	δ_o
A400	0.024	1.67±0.75	14.80	3.50±0.87
A1314	0.034	1.16±0.53	15.24	5.33±1.02
A1367	0.022	1.67±0.75	14.45	3.00±0.82
A1836	0.036	1.00±0.45	15.54	3.10±0.64
A2063	0.035	1.00±0.45	15.34	4.38±0.82
RXCJ2315.7-0222	0.027	0.33±0.15	14.61	2.00±0.71
A2877	0.025	1.16±0.53	14.39	none
A3581	0.023	0.67±0.30	14.54	none
AS137	0.026	1.67±0.75	14.63	none
AS758	0.038	1.16±0.53	15.64	none

sources per degree square for the Lockman Hole Field. We calculated 53±8 sources per degree square for Hubble Deep Field North at this flux value. X-ray source overdensities have been computed using the equation $1+\delta_x = N_x/N_e$ (Koulouridis & Plionis 2010), where N_x is the number of X-ray sources brighter than log S (-13.5 erg cm^{-2} s^{-1}) and N_e is expected X-ray source numbers from non-clustered fields. Optical overdensities were also calculated from the following equation $1+\delta_o = N_o/N$. In this formula, N_o is the number of objects with the characteristic magnitude of the selected galaxy cluster within the field of view and N is the total number of objects from non-clustered fields with the same characteristic magnitude. Due to minimisation of projection effects, all galaxies around the cluster centre were extracted by using the method explained by Koulouridis & Plionis (2010) (see section 3.2). Eventually, we calculated optical galaxy overdensities by using characteristic magnitude approximation with optical data. The characteristic magnitude of our clusters within range of m^*_r ±2.0 was estimated by using the following equation $m^* = M^* + 5\log(d) + K(z) + 25 + A_v$, where M^* is fit parameter from Schechter Luminosity function for r band (Montero-Dorta & Prada 2009), A_v is the galactic absorption, which is estimated from galactic absorption map (Schlafly & Finkbeiner 2011), and K(z) is the K-correction factor (Poggianti 1997). We also remind that classified stars and foreground/background galaxies were not taken into consideration in our analysis. Overdensity results of our samples are presented in Table 3.

5   DISCUSSION

We performed data analysis for *XMM-Newton* observations of a sample of clusters and fields. Log N - Log S was studied at limiting flux value of 1×10^{-14} erg cm^{-2} s^{-1} and, we found ∼ 2 times higher X-ray source density from our clusters compared to the values calculated in the Hubble Deep Field North and those estimated in the Lockman hole field studied by Hasinger et al. (2001) (see Fig. 2). Even in the worse case scenario according to the error limits, at least % 35 of our point sources are cluster members. Due to minimise the influence of ICM, we did not take into account the central regions of our clusters in our analysis. Also, we studied
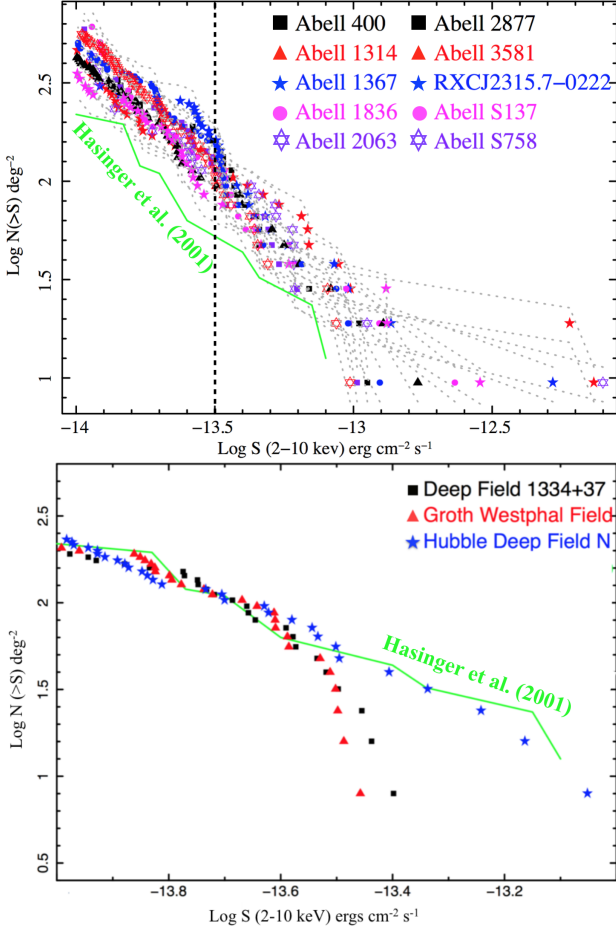
Figure 2. Log N - Log S calculated in the 2-10 keV band for our sample of clusters (**Top**) and our sample of fields (**Bottom**). The grey dotted lines represent a 1σ statistical error. The black dashed lines demonstrate $\log(f)$ = -13.5 erg cm^{-2} s^{-1} value for visual aid, which we used in our X-ray overdensity measurements. The green lines represent Lockman Hole results, which is studied by Hasinger et al. (2001).

three different fields to enlarge our knowledge about non-clustered fields. The number counts, which were calculated in the Lockman Hole and our field samples are consistent with each other, and we confirm lower X-ray source densities in non-clustered fields than in galaxy clusters (see Fig. 2). Encouraged by this result, we calculated X-ray to optical flux ratio to understand the variety of X-ray sources detected in clusters. R-band magnitudes were compared to hard X-ray flux values and X/O were calculated by using the equation $X/O = \log(f_X) + C + m_{opt} \times 0.4$ (Maccacaro et al. 1998). R-band magnitudes are taken from SDSS, NOMAD and MORX catalogue, and we applied extinction correction by using extinction maps from Schlafly & Finkbeiner (2011). Comparison between r-band magnitudes and X-ray fluxes is an advantageous method to address the condition of nuclear activity/inactivity of galaxies. Whereas AGNs tend to have X/O>-1 (e.g., Fiore et al. 2003), normal galaxies have X/O <-2 (e.g., Xue et al. 2011). Besides, galaxies with -2 < X/O < -1 value can either be LLAGNs or star-forming galaxies (Park et al. 2008). However, we cannot completely explain the type of the source due to the X-ray versus optical flux ra-

tio. Therefore, we calculated X-ray to optical luminosity ratio for 40 member galaxies, and the results are given in Table A1. Matsushita (2001) studied early type galaxies and found the expected L_X/L_B distribution of normal early type galaxies. Ranalli et al. (2005) also reported the expected L_X/L_B distribution of late-type galaxies. We compared hard band X-ray luminosities (2 -10 keV) to blue optical luminosities to understand the behaviour of our cluster member galaxies. Absolute magnitudes were computed using the equation: $M_{opt} = m_{opt} + 5 - 5\log(d)$, where d is the distance in parsec unit, m_{opt} is apparent magnitude value. Optical luminosities in solar units were calculated by using the equation $\log(L_{opt}/L_\odot) = -0.4 \times (M_{opt} - C)$, where C is absolute magnitude of the sun in the related band. The majority of our sources has significantly higher L_X/L_B than early type galaxies. Furthermore, ~ %50 of our member galaxies follow expected L_X/L_B distribution of late type galaxies. Based on our L_X/L_K results, we found that majority of the member galaxies is brighter in the X-rays than they are in the K band. The trends with L_B and L_K of L_X plots are presented in Fig. 3. Moreover, we assumed our point sources as likely cluster member and calculated luminosity values of our point sources by using cluster's redshifts. The luminosity range of our X-ray sources are found to be faint (40.08 $\leqslant \log(L_X) \leqslant$ 42.39 erg s^{-1}). In this luminosity range, the X-ray emission can be produced by either LLAGNs, star formation and unresolved XRBs. We also note that the majority of X-ray sources of our survey is found to be normal or star-forming galaxies ($\log(L_X)$ < 41.00 erg s^{-1}) (see Tables B2, B3, B4, B5, B6, and B7). This result implies no central nuclear activity from these sources. Early studies of the local Universe demonstrate that XRB populations dominate X-ray emission from normal galaxies (e.g., Muno et al. 2004), which can be the main X-ray emission mechanism of normal galaxies in our survey.

5.1 The contribution from LLAGNs

Based on our results, there is a possibility of AGN fuelling and quenching scenario in our clusters. When a galaxy falls into cluster environment under the influence of gravitational potential, the surrounding gas powers AGN (Lietzen et al. 2011), therefore, the source becomes brighter. Most of the galaxies host a black hole at the centre (Kormendy & Richstone 1995), and possible fuelling from ICM activates inactive Black Holes (e.g., Alexander & Hickox 2012). Besides, close encounters and collisions of galaxies are highly probable in cluster environments, where close encounters possibly cause AGN triggering (Ellison et al. 2011). Our results show the suppression of X-ray AGNs in the central regions of clusters (see Fig. 4, 5, 6). It appears that high pressurised winds from the cluster's centre affect the balance of galaxies within cluster environment and cause them to lose significant amounts of their fuel. This mechanism also explains the absence of very luminous galaxies at $L_X \geqslant 10^{42}$ erg s^{-1} in nearby clusters. In this case, LLAGNs in nearby cluster environments can be related to close encounters of galaxies rather than AGN fuelling.
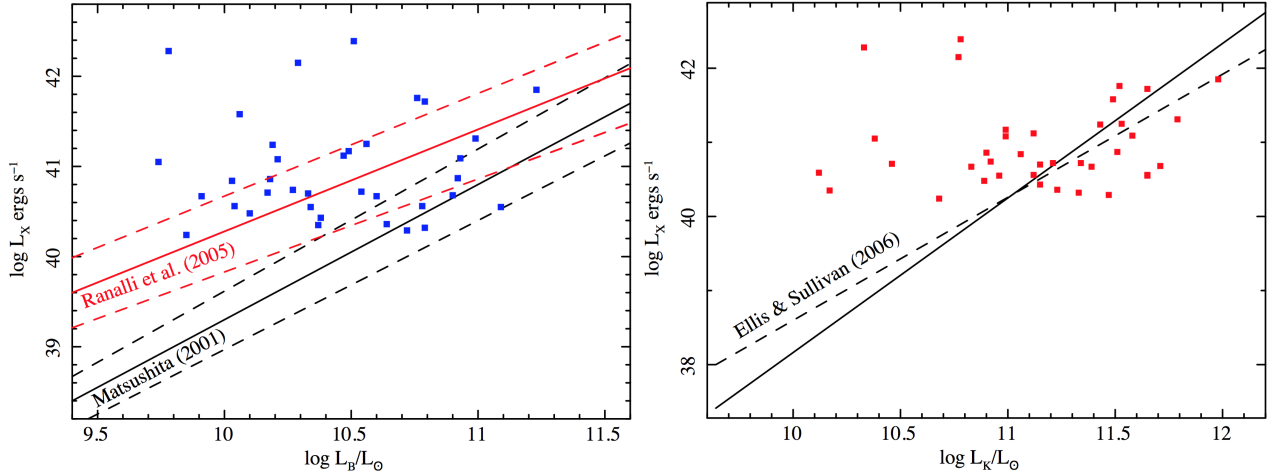
Figure 3. Top: L_X as a function of L_B for our galaxies within the cluster environment. The black solid line represents the expected distribution of early-type galaxies reported by Matsushita (2001), while the black dashed lines mark the $\pm10\%$ uncertainties on the relation. The red solid line represents the expected distribution of late type galaxies reported by Ranalli et al. (2005), while the red dashed lines mark the $\pm8\%$ uncertainties on the relation. **Bottom:** L_X as a function of L_K for our galaxies within the cluster environment, compared to results reported by Ellis & O'Sullivan (2006). The black solid line shows the best-fit to their early type galaxies sample, while the black dotted line represents the expected distribution of early-type galaxies in non-clustered fields.

5.2 Star formation

A considerable number of recent studies reports that star formation rate increases through cluster outskirts, however star formation rates of galaxies are still lower than the field even at the viral radius of clusters of galaxies (e.g., Balogh et al. 1999; Lewis et al. 2002; Muzzin et al. 2008; Wagner et al. 2017). On the other hand, it is well known that old red galaxies dominate cluster centres (e.g., Dressler 1980); however, blue galaxies are also commonly detected in clusters. Several studies indicate that there is a significant relation between galaxy colour and star formation (e.g., Tojeiro et al. 2013), whereas blue galaxies with high SFR are bright in X-ray (e.g., Fabbiano 1982). Encouraged by this relation, we studied the colour properties of the optical counterparts of the point-like sources in our sample. In Table B1, we classify our bright X-ray sources (log $f_X \geqslant$ -13.5 erg cm^{-2} s^{-1}) by their optical colour bi-modality by using the g-r/r or B-R/R methods (see section 3.3). We used these parameters to get indications on the nature of X-ray emission in our galaxies. We found that the number of the red and blue galaxies is approximately equal ($N_R \approx N_B$) (see Fig. 1), and $\sim$ %55 of the optical counterparts of the X-ray bright sources are identified as blue galaxies. On the other hand, a considerable number of our galaxies is found to be star-forming galaxies (see Fig. 3). Because the most massive, short-lived, newly-formed stars can become high mass X-ray binaries (HMXB) that remain bright for $\sim 10^{6-7}$ yr, the total X-ray emission closely tracks the star formation rate (e.g., Helfand & Moran 2001). However, it is not possible to separate X-ray emission from HMXBs and LMXBs in distant galaxies. We note that low mass X-ray binary (LMXB) populations are quite low in late-type galaxies (e.g., Grimm et al. 2005; Fabbiano 2006). In this case, the large number of the HMXBs might cause luminous X-ray emission ($10^{40} < L_X < 10^{42}$ erg s^{-1}) from these sources. However, we also note that high X-ray emission from late-type galaxies ($L_X > \times 10^{41}$ erg s^{-1}) can also

be produced by nuclear activity and a large population of XRBs at the same time. In some cases, supernova remnants (SNRs) can make small contributions to X-ray emission at lower luminosities.

5.3 Galaxy evolution within environment

We studied X-ray overdensities from galaxy clusters relative to non-clustered fields. Expected X-ray source number densities were calculated in the Hubble Deep Field North, where number densities from fields are consistent with other field samples (see Fig. 2). We used SDSS archival data to obtain optical overdensities for 6 of the clusters in our sample, however, there are no SDSS observations for the remaining number of clusters. Optical galaxy overdensities were calculated in two divided areas by using characteristic magnitude method described in detail (see section 4). X-ray and optical overdensities were compared with each other to address the nature of point-like X-ray emission. As a result, X-ray overdensities are found to be significantly lower than optical overdensities in our calculations (see Table 3). However, we also point out that the X-ray overdensity of A1367 surprisingly reaches the mean optical overdensity at the outskirts of the cluster. This cluster shows an elongated shape through NW-SE direction, and two groups of star-forming galaxies are falling into the cluster's centre (Cortese et al. 2004). Recent studies imply that increased galaxy X-ray emission from cluster's field is probably caused by occurring merger events. Neal & Frazer (2003) reported triggered AGN activity from A2255 due to a cluster-cluster merger. Also, Hwang & Lee. (2009) studied two merging galaxy clusters and reported that cluster member galaxies show increased X-ray emission that can be related to both star formation and AGN activity. Therefore, member galaxies of A1367 are possibly triggered by ongoing merger events or in-falling of X-ray bright object that probably increased X-ray overdensity at the outskirts of A1367. In Figs 4, 5, and 6 we demonstrate

the X-ray to optical overdensity comparisons as a function of radius. As can be seen from these figures, the optical galaxy densities decrease through outskirts of our clusters, whereas X-ray overdensities increase through outskirts. Our results reveal that X-ray sources are suppressed within the cluster environment, and suppression of X-ray AGNs increases through cluster's centre.

6 NOTES ON POINT-LIKE SOURCES

In this section, we will present the results of an analysis meant to identify the main X-ray emission process (i.e., AGN or star formation) in a sub-sample of point-like sources. We present optically identified cluster members in Table A1. In Table B1, we present X-ray/optical properties of point sources by assuming them as likely cluster member. At low X-ray luminosities ($10^{41} < L_X < 10^{42}$ erg s^{-1}), it is not clear whether X-ray emission comes from SF or LLAGN. Therefore, measurement of SFR by using different methods can be very effective to resolve the nature of X-ray emission. We calculated the SFR of point sources by using the equations defined by (Condon et al. 1992) and (Ranalli et al. 2003) respectively:

$$SFR[M \odot y^{-1}] = 2.5 \times 10^{-29} \times L_{1.4GHz}(erg s^{-1} Hz^{-1}) \quad (2)$$

$$SFR[M \odot y^{-1}] = 2 \times 10^{-40} \times L_{2-10keV}(erg s^{-1}) \quad (3)$$

6.1 The member galaxies

3C 75A is identified as a pair member of NGC 1128 and the brightest galaxy of A400 (Lin & Mohr 2004). This galaxy is elliptical and emits radio frequencies from relativistic jets (Bridle & Perley 1984). Spectrum of this source contains absorption and thermal emission lines, and the best fit parameters are Γ=1.70±0.11, $norm_{pow}$= (8.28±2.52) × 10^{-6} cm^{-5}, nH=0.52±0.18 cm^{-2}, kT=0.8±0.05 keV, and $norm_{apec}$ = (6.76±2.18) × 10^{-5} cm^{-5}. Besides, X-ray hardness ratio is measured as -0.42±0.08. Furthermore, X-ray to optical comparison reveals a bright X-ray emission (log L$_X$ = 41.25) from this source. By considering all these facts, we predict that X-ray emission mostly comes from central AGN. **NGC 3860** is identified as a strong AGN (possibly triggered by super-massive black hole) by Gavazzi et al. (2011). We calculated X/O = -1.64, log(L$_X$/L$_B$) = 30.68 and log(L$_X$/L$_K$)=30.23. Fitting the X-ray spectrum with a (Γ = 1.30±0.14), fixed column density (nH = 1.82 × 10^{20} cm^{-2}) and redshift (z=0.018663), we found a hardness ratio (HR) = -0.44±0.17 and log L$_X$ = 41.17 erg s^{-1}. According to these results, we claim that the X-ray emission process in NGC 3860 is due to nuclear activity, even though the source is an LLAGN. **NGC 3862** is classified as brightest cluster galaxy (BCG) (Sun 2009) and AGN (Véron-Cetty & Véron 2010; Gavazzi et al. 2011) due to its optical properties. Our results also reveal possible low luminous AGN activity (log L$_X$ = 41.76 erg s^{-1}) from this source (see Table A1). **MCG+08-21-065** is a spiral galaxy (Sb)(Miller & Owen 2010), and radio source (NVSS J113543+490214) is associated with this galaxy (Condon et al. 1998). Our

analysis reveals very bright X-ray emission (log L$_X$ =42.15 erg s^{-1}) from this source. Therefore, MCG+08-21-065 is an AGN. Shirazi & Brinchmann (2012) studied the optical spectrum of **2MASX J11340896+4915162** and classified this source as an AGN. On the basis of our results, we calculated log L$_X$ = 42.28 erg s^{-1} and high X-ray to optical flux ratio (X/O = -0.22) for this source. We confirm this source as AGN. **2MASX J15231224+0832590** is identified as a spiral galaxy (Sa) (Leaman et al. 2011). Spectral analysis of this source results in a Γ = 1.63±0.12, logarithmic X-ray luminosity log L$_X$ = 42.40 erg s^{-1}, and hardness ratio (HR) = 0.35±0.04. In considering these results, we identify this source as an AGN. **ESO 510- G 066** is identified as a lenticular galaxy (Sa0) (Vaucouleurs et al. 1991), and show shreds of evidence of radio jets (Van Velzen et al. 2012). Spectral analysis of this source demonstrated that this source is an unabsorbed X-ray source, where Γ = 2.33±0.4. The investigation reveals enhanced X-ray emission with high X-ray to optical flux/luminosity ratio (X/O = -1.88). Furthermore, log L$_X$ = 41.24 erg s^{-1} and hardness ratio = -0.75±0.03 were calculated for this source. This galaxy is located in the outskirt of the A3581, and the X-ray centroid has a positional offset (~ 1.5 kpc) relative to the optical centroid. We calculated the star formation rate = 34.76 M$_\odot$/yr for a given X-ray luminosity of 41.24. This SFR measurement is in agreement with the one from the 1.4 GHz flux (SFR = 36.98 M$_\odot$/yr). By considering all these facts, we classify the source as a star-forming galaxy. **NGC 3860B** is a spiral galaxy (S) and classified as HII region-like galaxy (Gavazzi et al. 2011). As expected from H II region-like galaxies, this source appears to emit UV emission (Marcum et al. 2001). In addition, Thomas et al. (2008) studied the H$_\alpha$ properties of this galaxy and reported SFR = 2.0 M$_\odot$/yr. The SFR values we computed using the radio and X-ray luminosities are in good agreement with the UV measurements, being 3.47 M$_\odot$/yr and 4.48 M$_\odot$/yr respectively. In conclusion, NGC 3860B appears to be X-ray normal galaxy.

6.2 New LLAGN candidates

In this section, we concentrate on identifying new possible low luminous AGNs from our survey. To define LLAGNs, we studied X-ray properties, X/O, galaxy colour and hardness ratio of point sources. Hardness ratio is defined as (H-S)/(H+S), where H is count rate in 2.0-10.0 keV band and S is count rate in 0.5-2.0 keV band. We present seven new LLAGN candidates in Table 4. LLAGN selection is performed using following indicators:

- X/O (> -1)
- Galaxy colour (Red)
- Hardness ratio (> -0.55)
- Total X-ray counts (> 100 cts)
- X-ray luminosity (> 10^{41} erg s^{-1})

These indicators are very efficient to identify X-ray AGNs, and similar methods were applied to other AGN candidates on different surveys (e.g., Xue et al. 2011; Ranalli 2012; Vattakunnel et al. 2012; Marchesi et al. 2016).
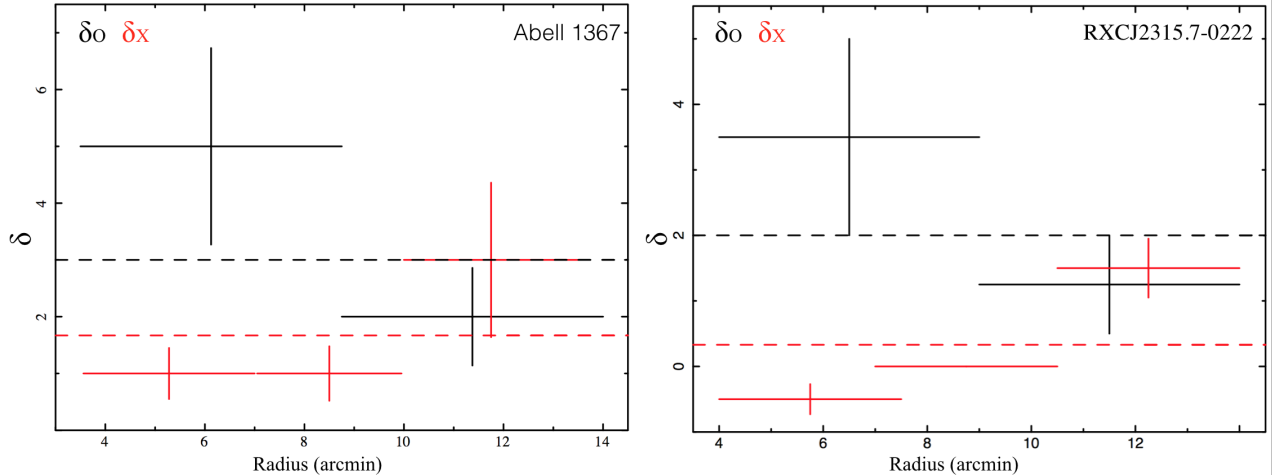
Figure 4. X-ray versus optical overdensity as a function of the distance from the centre of the cluster. The red dashed line corresponds to the mean X-ray overdensity of relative galaxy cluster, and the black dashed line represents optical overdensity of relative galaxy cluster.

Table 4. X-ray to optical properties of new LLAGN candidates.

Source Name	HR	$\log(L_X)$ erg s^{-1}	X/O	Cluster
XMMU J140721.6-264716	0.62±0.11	41.30	-0.68	A3581
XMMU J113408.4+490318	-0.54±0.07	41.24	-0.02	A1314
XMMU J140215.6-113748	-0.07±0.05	41.84	0.21	A1836
XMMU J011105.5-612548	0.29±0.11	41.16	-0.61	AS137
XMMU J010949.4-613153	-0.33±0.09	41.13	0.02	AS137
XMMU J141216.6-342422	-0.45±0.04	41.46	-0.10	AS758
XMMU J141308.6-342105	0.30±0.22	41.49	-0.96	AS758

7 CONCLUSIONS

In this work, we studied ten nearby ($\leqslant$ 171 Mpc) galaxy clusters. Within these clusters, we detected 874 point-like sources; a fraction of them (483) is expected to be a false detection related to the diffuse ICM emission. We removed those sources located in the central regions of galaxy clusters (95 $\leqslant$ r_c $\leqslant$ 145 kpc) from our final sample unless they are bright enough to be detected within ICM. All the point-like sources within 0.3-10 keV spectra were fitted with an absorbed power-law; a minority of spectra showed evidence of thermal emission lines, which we fitted adding a thermal component (APEC). We calculated the log N - log S for our samples and we compared cluster results with those obtained in the Lockman Hole and in the Hubble Deep Field North. The number counts are a factor $\sim$ 2 higher in the clusters than they are in the fields, at any flux level. In the luminosity range ($40.08 \leqslant \log(L_X) \leqslant 42.39$ erg s^{-1}) of the point-like sources in our sample, X-ray emission is mostly produced from LLAGNs, XRBs and star formation. Although starburst and normal galaxies dominate large fraction of X-ray sources of our survey, the fraction of LLAGNs is nonetheless significant. Using proxies such as X/O, L_X/L_B and L_X/L_K, we found significant X-ray excess in several galaxies. By considering X-ray excess of member galaxies, we linked the nature of X-ray emission to two different processes: AGN triggering and star formation. We used efficient indicators to separate LLAGNs and star-forming galaxies. In the major-

ity of the red galaxies, the enhanced X-ray emission can be explained by AGN activity; nevertheless X-ray emission can be produced by unresolved XRBs in some cases. For the blue galaxies, we explained X-ray excess with star formation, which can be related to an extreme number of HMXBs and/or contributions from SNRs. Due to the absence of redshift information of X-ray sources, we assumed all X-ray sources in our survey as cluster members, and we compared X-ray and optical overdensities of our sample of clusters. We found that X-ray overdensities are significantly lower than optical overdensities in our survey, which can be explained by the fact that X-ray sources are suppressed within cluster environments. We also note that some non-redshift X-ray sources may not be cluster members. In that case, calculated X-ray overdensities may decrease, and suppression of X-ray sources in cluster environments even becomes clearer. The absence of very bright X-ray sources ($L_X > 10^{42}$ erg s^{-1}) in nearby galaxy clusters indicates that X-ray AGNs are the highly suppressed within the central regions of clusters due to highly pressurised environment. We still note that although dense and hot ICM suppress X-ray AGNs, AGN fuelling can still be effective in the sparse parts of ICM. As possible as this scenario is, we conclude that the large majority X-ray bright galaxies at the outskirts of clusters are dominated by star formation activities. Furthermore, we explain the existence of LLAGNs within clusters with close encounters of galaxies rather than AGN fuelling. Consequently, we contributed the suppression/triggering conflict in favour of the suppression by studying ten nearby galaxy clusters. However, the number of clusters in our sample is quite low, and more SDSS and XMM-Newton observations of nearby galaxy clusters are required to solve the conflict.

Figure 5. X-ray versus optical overdensity as a function of the distance from the centre of the cluster. The red dashed line corresponds to the mean X-ray overdensity of relative galaxy cluster, and the black dashed line represents optical overdensity of relative galaxy cluster.
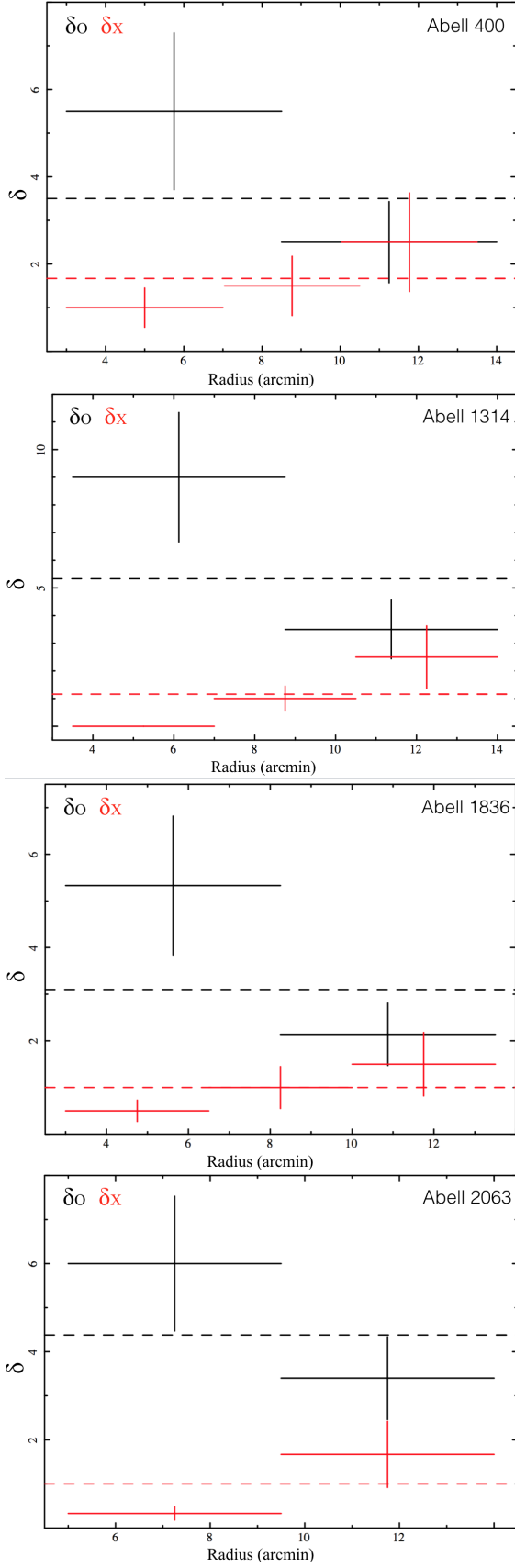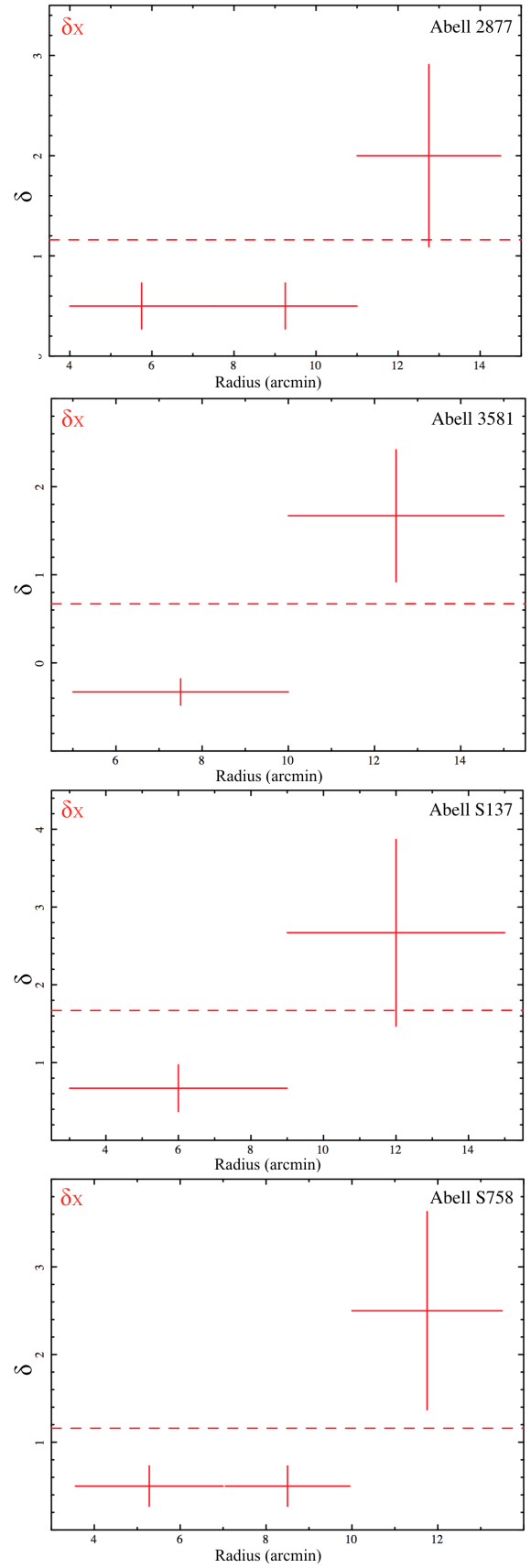
Figure 6. X-ray versus optical overdensity as a function of the distance from the centre of the cluster. The red dashed line corresponds to the mean X-ray overdensity of relative galaxy cluster, and the black dashed line represents optical overdensity of relative galaxy cluster.

REFERENCES

Alberts S., et al., 2016, ApJ, 825, 72

Alexander D. M., Hickox R. C., 2012, NewAR, 56, 93

Balogh M. et al., 1997, ApJ, 488, 75

Balogh M. et al., 1999, ApJ, 527, 54

Bufanda E. et al., 2017, MNRAS, 465, 2531

Brusa M. et al., 2010, ApJ, 716, 348

Bridle A. H., Perley R. A., 1984, ARAA&A, 22, 319

Butcher H., Oemler A., 1978, ApJ, 226, 559

Cappelluti N. et al., 2005, A&A, 430, 39

Cappi M. et al., 2001, ApJ, 548, 624

Condon J. J., 1992, ARA&A, 30, 575

Condon J. J. et al. 1998, AJ, 115, 1693

Cortese L., Gavazzi G., Boselli A., Iglesias-Paramo J., Carrasco L., 2004 A&A, 425, 429

Dai X., Griffin R. D., Kochanek C. S., Nugent J. M., Bregman J. N., 2015, ApJs, 218, 8

Dalya G. et al., 2016, VizieR Online Data Catalog, 7275

D'Elia V. et al., 2004, NuPhS, 132, 54

Dressler A., 1980, ApJ, 236, 351

Dressler A. et al., 1999, ApJs, 122, 51

Ehlert S. et al., 2013, MNRAS, 428, 3509

Ehlert S. et al., 2014, MNRAS, 428, 3509

Ellis S. C., O'Sullivan E., 2006, MNRAS, 367, 627

Ellison S. L., Patton D. R., Mendel J. T., Scudder J. M., 2011, MNRAS, 418, 2043

Fabbiano G., Feigelson E., Zamorani G., 1982, ApJ, 259, 367

Fabbiano G., 2006, ARA&A, 44, 323

Fassbender R., Šuhada R., Nastasi A., 2012, AdAst, 2012, 32

Fiore F. et al., 2003, A&A, 409, 79

Flesch E., 2010, PASA, 27, 283

Gavazzi G., Savorgnan G., Fumagalli M., 2011, A&A, 534, 31

Getman, K. V. et al., 2005, ApJs, 160, 319

Gilmour R., Best P., Almaini O., 2009, MNRAS, 392, 1509

Gisler, G. R. 1978, MNRAS, 183, 633

Grimm H. J., McDowell J., Zezas A., Kim D. W., Fabbiano G., 2005, ApJS, 161, 271

Haggard D. et al., 2010, ApJ, 723, 1447

Haines C. P. et al., 2012, ApJ, 754, 97

Hasinger G. et al., 2001, A&A, 365, 45

Helfand D. J., Moran E. C., 2001, ApJ, 554, 27

Ho L. C. et al., 2001, ApJ, 549, 51

Hudaverdi M. et al., 2006, PASJ, 58, 931

Hwang H. S., Lee M. G., 2009, MNRAS, 397, 2111

Kauffmann G. et al., 2003, MNRAS, 341, 33

Kauffmann G. et al., 2004, MNRAS, 353, 713

Khabiboulline E. T. et al., 2014, ApJ, 795, 62

King I., 1962, AJ, 67, 471

Kormendy J., Richstone D., 1995, ARA&A, 33, 581

Koulouridis E., Plionis M., 2010, ApJ, 714, 181

Koulouridis E. et al., 2014, A&A, 567, 83

Koulouridis E. et al., 2016, A&A, 592, 11

Laganá T. F., Dupke R. A., Sodré L. Jr., Lima Neto G. B., Durret, F., 2009, MNRAS, 394, 357

LaMassa S. M. et al., 2013, MNRAS, 436, 3581

Leaman J., Li W., Chornock R., Filippenko, A. V., 2011, MNRAS, 412, 1419

Lewis I. et al., 2002, MNRAS, 334, 673

Lietzen H., et al., 2011, A&A, 535, 21

Lin Y., Mohr J. J., 2004, ApJ, 617, 879

Loaring N. S. et al., 2013, MNRAS, 362, 1371

López-Cruz O., Barkhouse W. A., Yee H. K. C., 2004, ApJ, 614, 679

Maccacaro T. et al., 1998, ApJ, 326, 680

Marchesi S. et al, 2016, ApJ, 817, 34

Martini P., Kelson D. D., Kim E., Mulchaey J. S., Athey A. A., 2006, AJ, 644, 116

Masters K. L. et al., 2010, MNRAS, 405, 783

Matsushita K., 2001, ApJ, 547, 693

Marcum P. M. et al., 2001, ApJS, 132, 129

Melnyk O. et al., 2013, A&A, 557, 81

Mineo S., Gilfanov M., Sunyaev R., 2012, MNRAS, 419, 2095

Montero-Dorta A. D., Prada F., 2009, MNRAS, 399, 1106

Muno M. P. et al., 2004, ApJ, 613, 1179

Muzzin A., Wilson, G., Lacy, M., Yee, H. K. C., Stanford, S. A., 2008, ApJ, 686, 966

Miller N. A., Owen F. N., 2003, AJ, 125, 2427

Neal A. M., Frazer N. O., 2003, ApJ, 125, 5

Oemler A. Jr, 1974, ApJ, 194, 1

Park S. Q. et al., 2008, APJ, 678, 744

Peres, C. B. et al., 1998, MNRAS, 298, 416

Pimbblet K. A. et al., 2002, MNRAS, 331, 333

Popesso P., Biviano A., 2006, A&A, 460, 23

Pineau F. X. et al., 2011, A&A, 527, 126

Poggianti B. M., 1997, A&AS, 122, 399

Ranalli P., Comastri A., Setti G., 2003, A&A, 399, 39

Ranalli P., Comastri A., Setti G., 2003, A&A, 440, 23

Ranalli P. et al., 2012, A&A, 542, 16

Ruderman, J. T., Ebeling, H., 2005, APJ, 623, 81

Schaefer A. L. et al., 2017, MNRAS, 464, 121

Schlafly E. F., Finkbeiner D. P., 2011, ApJ, 737, 103

Shirazi M., Brinchmann J., 2012, MNRAS, 421, 1043

Sun M., 2009, ApJ, 704, 1586

Thomas C. F. et al., 2008, A&A, 486, 755

Tojeiro R. et al, 2013, MNRAS, 432, 359

Tully R. B., Mould J. R., Aaronson M., 1982, ApJ, 257, 527

Tully R. B., 2015, AJ, 2015, 149, 171

Van den Bergh S., 1976, ApJ, 206, 883

Van Velzen S. et al, 2012, A&A, 544, 18

Vattakunnel S. et al., 2012, MNRAS, 420, 2190

de Vaucouleurs G. et al., 1991, RC3, 9, 0

Véron-Cetty M. P., Véron P., 2010, A&A, 518, 10

Wagner C. R. et al., 2017, ApJ, 834, 53

Wetzel A. R., Tinker J. L., Conroy C., van den Bosch F. C., 2014, MNRAS, 439, 2687

Xue Y. Q. et al., 2011, ApJs, 195, 10

Zacharias N. et al., 2005, AAS, 205, 4815

Zacharias N. et al., 2013, AJ, 145, 44

Table A1. X-ray to optical properties of individual galaxies.

Object Name (I)	Redshift (II)	m_r (III)	X/O (IV)	m_B (V)	m_K (VI)	log L_X (VII)	$\log(L_K/L_\odot)$ (VIII)	log $(L_B/L_\odot)$ (IX)	Type (X)	Cluster (XI)
CGCG 415-040	0.022980	14.35	-2.19	14.53	10.34	40.70	11.15	10.33	S0	A400
CGCG 415-046	0.022820	14.50	-2.28	14.48	10.79	40.55	10.96	10.34	E	A400
3C 75A	0.022580	14.99	-1.48	13.86	9.32	41.25	11.53	10.56	E	A400
3C 75B	0.024113	13.10	-2.66	15.00	12.15	40.71	10.46	10.17	S0	A400
2MASX J02574741+0601395	0.024811	15.09	-1.93	15.72	11.29	40.67	10.83	9.91	E	A400
2MASX J01100662-4555544	0.024360	15.46	-1.38	16.14	12.42	41.05	10.38	9.74	S0	A2877
2MASX J01101993-4551184	0.023243	none	none	15.31	10.61	40.84	11.06	10.03	S0	A2877
IC1633	0.024240	12.95	-2.14	12.40	8.39	41.85	11.98	11.23	E1	A2877
ESO 243- G 049	0.022395	14.29	-1.77	14.77	10.70	41.08	10.99	10.21	Sa0	A2877
ESO 243- G 051	0.021855	14.00	-2.68	13.62	10.01	40.36	11.23	10.64	Sb	A2877
ESO 243- G 045	0.025881	13.81	-2.25	13.32	9.71	40.87	11.51	10.92	S0	A2877
NGC 3851	0.021130	14.41	-2.29	15.12	11.01	40.48	10.89	10.10	E	A1367
NGC 3860	0.018663	14.32	-1.64	13.77	10.39	41.17	10.99	10.49	Sa	A1367
NGC 3860B	0.028250	15.69	-1.91	14.99	13.35	40.35	10.17	10.37	S	A1367
NGC 3861	0.016900	13.88	-2.42	12.93	9.95	41.12	11.12	10.78	S	A1367
NGC 3862	0.021718	13.64	-1.37	13.51	9.48	41.76	11.52	10.76	E	A1367
CGCG 097-125	0.027436	15.06	-1.77	15.23	11.46	40.74	10.92	10.27	E	A1367
NGC 3842	0.021068	12.18	-3.12	12.62	9.07	40.55	11.65	11.09	E	A1367
GALEXASC J114359.29+195633.6	0.023323	19.74	-0.08	21.38	none	40.56	none	7.67		A1367
2MASX J15225650+0839004	0.03361	15.00	-2.09	15.84	11.91	40.86	10.90	10.18	S0	A2063
CGCG 077-097	0.034174	13.14	-1.96	14.36	10.07	41.72	11.65	10.79	S?	A2063
2MASX J15231224+0832590	0.036619	15.20	-0.49	15.20	12.41	42.39	10.78	10.51	Sa	A2063
MCG -02-36-002	0.037776	12.74	-2.61	14.10	9.97	41.31	11.79	10.99	Sa0	A1836
2MASX J14015570-1138043	0.036979	16.57	-1.79	18.15	14.09	40.59	10.12	9.35		A1836
2MASX J14013206-1139261	0.041662	15.55	-1.74	15.60	11.86	41.12	11.12	10.47		A1836
IC 708	0.031679	13.07	-2.54	13.85	10.09	41.09	11.58	10.93	E	A1314
IC 711	0.032436	13.88	-2.59	14.88	11.08	40.72	11.21	10.54	E?	A1314
IC 712	0.033553	13.13	-2.98	14.05	9.89	40.68	11.71	10.90	S?	A1314
2MASX J11340896+4915162	0.037230	16.25	-0.22	16.99	13.47	42.28	10.33	9.78		A1314
MCG+08-21-065	0.029670	15.14	-0.58	15.21	11.88	42.15	10.77	10.29	Sb	A1314
LEDA 97398	0.031600	19.70	-0.38	20.80	none	40.65	none	8.11		A1314
IC 4374	0.021798	13.79	-1.44	15.24	9.54	41.58	11.49	10.06	Sa0	A3581
ESO 510- G 065	0.025671	14.21	-2.76	16.11	11.90	40.24	10.68	9.85	Sb	A3581
ESO 510- G 066	0.024333	13.78	-1.88	15.13	9.92	41.24	11.43	10.19	Sa0	A3581
MCG-06-31-029	0.038500	11.10	-3.89	11.20	11.15	40.72	11.34	12.17	E+	AS758
2MASX J14122917-3417417	0.043003	12.41	-3.49	15.36	11.24	40.67	11.39	10.60		AS758
NGC 0432	0.026929	13.82	-2.89	13.92	9.93	40.29	11.47	10.72	S0	AS137
2MASX J01125179-6139513	0.026442	14.05	-2.65	14.75	10.70	40.43	11.15	10.38	E	AS137
NGC 7556	0.025041	12.21	-3.23	15.39	9.24	40.56	11.65	10.04	S0	RXCJ2315.7-0222
NGC 7566	0.026548	13.03	-3.12	13.66	10.19	40.32	11.33	10.79	Sb?	RXCJ2315.7-0222

APPENDIX A: X-RAY TO OPTICAL PROPERTIES OF GALAXIES

X-ray and optical properties of identified member galaxies I) Galaxy names II) Redshift values from Ned Astronomical Database III) R-band magnitude values from Vizier database IV) X-ray to optical flux ratio V) Apparent blue magnitude values from Vizier database VI) Apparent k magnitude values are taken from Tully (2015); Dalya et al. (2016) VII) Hard band logarithmic X-ray luminosity values from spectral analysis VIII) K-band luminosities calculated from extinction corrected k-band magnitude. IX) Logarithmic blue optical luminosity values calculated from extinction corrected b-band magnitudes X) Morphological type of galaxies XI) Name of cluster hosts identified galaxies.

Table B1. Galaxy Colour Survey

Object Name	HR	Log f$_X$ erg cm^{-2} s^{-1}	Log L$_X$ erg s^{-1}	r mag	g-r mag	d Mpc	P %	Type	Cluster
I	II	III	IV	V	VI	VII	VIII	IX	X
XMMU J025824.6+060248	-0.61±0.05	-12.72	41.40	18.58	0.33	0.31	84	Blue	A400
XMMU J025749.2+055136	-0.49±0.09	-12.95	41.18	21.09	0.02	0.29	98	Blue	A400
XMMU J025747.3+060942	-0.54±0.13	-13.43	40.70	20.67	-0.04	0.24	91	Blue	A400
XMMU J025718.5+060022	-0.57±0.15	-13.34	40.76	20.73	0.59	0.17	92	Blue	A400
XMMU J025730.8+060545	-0.34±0.20	-13.44	40.69	18.53	0.64	0.15	97	Blue	A400
XMMU J025718.8+060813	-0.45±0.21	-13.48	40.65	17.60	0.84	0.25	96	Red	A400
XMMU J025806.2+055327	0.09±0.32	-13.31	40.82	20.91	0.02	0.29	95	Red	A400
XMMU J025712.6+055960	0.88±0.17	-13.42	40.71	21.07	0.66	0.21	96	Red	A400
XMMU J113421.6+490050	-0.60±0.08	-13.47	40.95	19.47	0.66	0.24	98	Blue	A1314
XMMU J113408.4+490318	-0.54±0.11	-13.16	41.24	19.09	1.01	0.28	83	Red	A1314
XMMU J113548.5+491150	-0.44±0.24	-13.48	40.93	20.95	0.48	0.49	95	Blue	A1314
XMMU J114435.0+195131	-0.58±0.08	-13.07	40.97	20.01	0.65	0.20	94	Blue	A1367
XMMU J114427.1+194338	-0.62±0.18	-13.32	40.72	21.09	0.45	0.09	89	Blue	A1367
XMMU J114452.5+195133	-0.55±0.10	-13.02	41.02	21.89	0.32	0.21	98	Blue	A1367
XMMU J114515.8+194951	-0.61±0.28	-13.38	40.66	19.84	0.27	0.28	97	Blue	A1367
XMMU J114436.5+195336	-0.29±0.30	-13.48	40.56	20.89	0.19	0.25	99	Blue	A1367
XMMU J114359.3+195632	-0.73±0.21	-13.48	40.56	21.75	0.70	0.30	73	Red	A1367
XMMU J114507.7+193552	-0.82±0.37	-13.49	40.55	21.27	1.09	0.31	92	Red	A1367
XMMU J140215.6-113748	-0.07±0.10	-12.63	41.84	18.36	1.05	0.37	96	Red	A1836
XMMU J140207.9-113553	-0.63±0.08	-13.42	41.06	19.53	0.11	0.28	94	Blue	A1836
XMMU J140135.5-112708	-0.15±0.34	-13.39	41.05	19.28	1.51	0.42	93	Red	A1836
XMMU J140043.8-113731	-0.29±0.40	-13.42	41.18	17.92	1.30	0.63	96	Red	A1836
XMMU J152342.5+084535	-0.82±0.32	-13.22	41.23	22.00	0.96	0.55	74	Red	A2063
XMMU J152250.9+084447	0.41±0.76	-13.21	41.21	21.34	1.15	0.38	92	Red	A2063
XMMU J152322.3+082159	-0.20±0.48	-13.22	41.23	19.99	0.23	0.64	97	Blue	A2063
XMMU J231638.6-022527	-0.56±0.07	-12.54	41.67	19.05	0.20	0.42	99	Blue	RXCJ2315.7-0222
XMMU J231624.5-021457	-0.77±0.07	-13.35	40.80	20.63	1.57	0.40	81	Red	RXCJ2315.7-0222
XMMU J231555.9-021644	0.33±0.29	-13.33	40.81	23.84	0.44	0.21	93	Blue	RXCJ2315.7-0222
XMMU J231610.3-021502	-0.64±0.31	-13.47	40.67	20.19	1.43	0.31	91	Red	RXCJ2315.7-0222
XMMU J231500.7-022515	-0.25±0.27	-13.36	40.85	18.72	0.72	0.34	97	Blue	RXCJ2315.7-0222

Object Name	HR	Log f$_X$ erg cm^{-2} s^{-1}	Log L$_X$ erg s^{-1}	R mag	B-R mag	d Mpc	P %	Type	Cluster
I	II	III	IV	V	VI	VII	VIII	IX	X
XMMU J010914.4-455914	-0.61±0.09	-13.02	41.13	18.98	0.74	0.23	93	Blue	A2877
XMMU J010952.4-460536	-0.63±0.26	-13.47	40.67	19.37	0.59	0.29	96	Blue	A2877
XMMU J011024.5-454426	-0.82±0.27	-13.44	40.70	18.97	0.48	0.36	98	Blue	A2877
XMMU J010858.9-455136	-0.01±0.49	-13.20	40.93	20.18	1.09	0.31	99	Red	A2877
XMMU J140721.6-264716	0.62±0.16	-12.77	41.30	16.47	1.65	0.40	92	Red	A3581
XMMU J140803.6-270841	-0.21±0.60	-13.49	40.58	20.17	1.31	0.31	85	Red	A3581
XMMU J140825.4-270849	-0.39±0.35	-13.25	40.82	20.17	0.71	0.42	85	Blue	A3581
XMMU J011205.4-613255	-0.56±0.09	-13.47	40.73	20.16	0.77	0.08	99	Blue	AS137
XMMU J011127.4-612612	-0.39±0.24	-13.49	40.70	18.35	0.87	0.18	99	Blue	AS137
XMMU J011105.5-612548	0.29±0.20	-13.02	41.16	17.28	1.63	0.24	88	Red	AS137
XMMU J010949.4-613153	-0.33±0.16	-13.06	41.13	18.95	1.57	0.44	62	Red	AS137
XMMU J011213.1-612015	-0.43±0.20	-13.36	40.84	19.34	0.49	0.37	99	Blue	AS137
XMMU J141117.5-341116	-0.58±0.16	-13.09	41.42	18.65	0.70	0.74	87	Blue	AS758
XMMU J141216.6-342422	-0.45±0.06	-13.06	41.46	18.65	1.70	0.19	93	Red	AS758
XMMU J141308.6-342105	0.30±0.22	-13.01	41.49	16.37	1.58	0.46	93	Red	AS758
XMMU J141245.4-342343	-0.46±0.10	-13.35	41.18	18.45	0.82	0.28	87	Blue	AS758
XMMU J141223.0-341330	-0.51±0.13	-13.47	41.06	18.65	0.50	0.32	88	Blue	AS758

APPENDIX B: GALAXY COLOUR - X-RAY POINT-LIKE EMISSION RELATION

I) Source name II) Hardness Ratio [defined as (H-S)/(H+S), where H is count rate in 2.0-10.0 keV and S is count rate in 0.5-2.0 keV] III) Logarithmic X-ray flux IV) Logarithmic X-ray luminosity V) R-band magnitude VI) G-R/B-R Values VII) Projected distance from centre of related galaxy cluster VIII) Likelihood of optical association IX) Galaxy type in colour X) Cluster name.

Table B2. Properties of point sources studied in this work.

Object Name	Net Counts	Log Flux erg cm^{-2} s^{-1}	Log Luminosity erg s^{-1}	Cluster	Optical Counterpart	Redshift
XMMU J025824.6+060248	750	-12.72	41.40	A400	2XMM J025824.6+060248	
XMMU J025741.5+060136	570	-12.98	41.25	A400	3C 75A	0.02258
XMMU J025741.8+060120	343	-13.40	40.71	A400	3C 75B	0.024113
XMMU J025749.2+055136	431	-12.95	41.18	A400	2XMM J025749.2+055136	
XMMU J025724.7+060156	481	-13.21	40.88	A400	2XMM J025724.7+060156	
XMMU J025808.1+055808	233	-13.34	40.76	A400		
XMMU J025747.3+060942	245	-13.43	40.70	A400		
XMMU J025802.5+055448	221	-13.47	40.67	A400		
XMMU J025802.3+055213	168	-13.67	40.47	A400		
XMMU J025718.5+060022	258	-13.34	40.76	A400		
XMMU J025736.7+060822	190	-13.58	40.55	A400		
XMMU J025730.8+060545	197	-13.44	40.69	A400		
XMMU J025718.8+060813	131	-13.48	40.65	A400		
XMMU J025803.6+061107	102	-13.49	40.64	A400		
XMMU J025806.2+055327	93	-13.31	40.82	A400		
XMMU J025820.9+060008	107	-13.65	40.48	A400		
XMMU J025747.1+060136	41	-13.47	40.67	A400	2MASX J02574741+0601395	0.024811
XMMU J025712.6+055960	132	-13.42	40.71	A400		
XMMU J025733.7+055835	244	-13.43	40.70	A400	CGCG 415-040	0.02298
XMMU J025716.6+055736	138	-13.66	40.47	A400		
XMMU J025821.0+060537	120	-13.58	40.55	A400	CGCG 415-046	0.02282
XMMU J025752.1+060631	97	-13.52	40.61	A400		
XMMU J025810.2+055948	148	-13.51	40.62	A400		
XMMU J025812.7+055828	83	-13.92	40.21	A400		
XMMU J025811.2+055227	78	-13.39	40.74	A400		
XMMU J025824.2+055810	58	-13.84	40.29	A400		
XMMU J025702.5+060945	63	-13.85	40.28	A400		
XMMU J025709.9+060320	69	-13.70	40.42	A400		
XMMU J025711.7+060160	92	-13.77	40.36	A400		
XMMU J025751.7+054843	49	-13.35	40.76	A400		
XMMU J025712.7+061114	60	-13.81	40.32	A400		
XMMU J025807.0+060155	74	-13.77	40.36	A400		
XMMU J025801.6+060148	67	-13.84	40.29	A400		
XMMU J010955.6-455551	1860	-12.82	41.85	A2877	IC1633	0.024240
XMMU J011050.6-460013	1245	-13.06	41.09	A2877	GALEX J011050.4-460013.8	
XMMU J010914.4-455914	443	-13.02	41.13	A2877	2XMM J010914.4-455914	
XMMU J011028.2-460422	401	-12.99	41.08	A2877	ESO 243- G 049	0.022395
XMMU J011119.3-455554	375	-13.78	40.36	A2877	ESO 243- G 051	0.021855
XMMU J011019.9-455120	90	-13.29	40.84	A2877	2MASX J01101993-4551184	0.023243
XMMU J010904.3-454627	97	-13.27	40.87	A2877	ESO 243- G 045	0.025881
XMMU J011007.5-455554	258	-13.07	41.05	A2877	2MASX J01100662-4555544	0.024360
XMMU J010942.5-455357	49	-13.90	40.24	A2877		
XMMU J011017.7-460404	108	-13.32	40.81	A2877		
XMMU J010949.1-460235	125	-13.72	40.42	A2877		
XMMU J010952.4-460536	130	-13.47	40.67	A2877		
XMMU J010916.4-454830	65	-13.58	40.56	A2877		
XMMU J011032.0-455337	178	-13.47	40.67	A2877		
XMMU J011024.5-454426	102	-13.44	40.70	A2877		
XMMU J010849.6-455622	91	-13.86	40.29	A2877		
XMMU J010930.7-460307	66	-13.65	40.47	A2877		
XMMU J010947.3-455327	98	-13.68	40.46	A2877		
XMMU J011026.6-455246	72	-13.60	40.54	A2877		
XMMU J010933.6-460400	42	-13.84	40.30	A2877		
XMMU J010935.8-460621	50	-13.46	40.68	A2877		
XMMU J011022.6-460105	86	-13.67	40.47	A2877		
XMMU J010853.8-455850	54	-13.77	40.37	A2877		
XMMU J011034.9-455149	100	-13.59	40.55	A2877		
XMMU J011008.8-455630	149	-13.37	40.76	A2877		
XMMU J011058.2-455318	70	-13.68	40.46	A2877		
XMMU J011001.9-454917	78	-13.62	40.52	A2877		
XMMU J011043.2-460419	103	-13.58	40.56	A2877		
XMMU J010937.2-454323	42	-13.61	40.53	A2877		
XMMU J010858.9-455136	104	-13.20	40.93	A2877		
XMMU J011001.7-460818	49	-13.75	40.39	A2877		
XMMU J011001.9-460335	63	-13.97	40.17	A2877		
XMMU J011006.8-455234	40	-13.53	40.61	A2877		
XMMU J011038.1-455829	41	-13.51	40.62	A2877		
XMMU J010916.1-455149	44	-13.51	40.63	A2877		

Table B3. Properties of point sources studied in this work.

Object Name	Net Counts	Log Flux erg cm^{-2} s^{-1}	Log Luminosity erg s^{-1}	Cluster	Optical Counterpart	Redshift
XMMU J114505.0+193622	3182	-12.28	41.76	A1367	NGC 3862	0.021718
XMMU J114435.0+195131	628	-13.07	40.97	A1367		
XMMU J114409.4+195009	576	-13.24	40.81	A1367		
XMMU J114448.9+194742	454	-12.86	41.17	A1367	NGC 3860	0.018663
XMMU J114427.1+194338	303	-13.32	40.72	A1367		
XMMU J114452.5+195133	515	-13.02	41.02	A1367		
XMMU J114515.8+194951	136	-13.38	40.66	A1367		
XMMU J114435.5+195029	146	-13.52	40.52	A1367		
XMMU J114503.8+195826	103	-13.48	40.56	A1367	NGC 3861	0.01690ă
XMMU J114436.5+195336	187	-13.48	40.56	A1367		
XMMU J114454.7+194634	175	-13.30	40.74	A1367	CGCG 097-125	0.027436
XMMU J114457.6+195302	145	-13.59	40.45	A1367		
XMMU J114436.5+193831	117	-13.52	40.52	A1367		
XMMU J114410.7+195327	100	-13.57	40.47	A1367		
XMMU J114359.2+193955	46	-13.42	40.61	A1367		
XMMU J114439.1+194525	167	-13.43	40.61	A1367		
XMMU J114416.8+194417	44	-13.48	40.56	A1367		
XMMU J114420.1+195849	41	-13.56	40.48	A1367		
XMMU J114438.1+194405	153	-13.45	40.59	A1367		
XMMU J114459.7+194742	96	-13.62	40.41	A1367		
XMMU J114422.1+193937	76	-13.46	40.58	A1367		
XMMU J114526.6+194345	43	-13.55	40.49	A1367		
XMMU J114420.9+195508	53	-13.71	40.32	A1367		
XMMU J114507.7+193552	74	-13.49	40.55	A1367		
XMMU J114447.3+194621	80	-13.69	40.35	A1367	NGC 3860B	0.02825
XMMU J114501.7+194549	93	-13.91	40.13	A1367		
XMMU J114536.9+195304	42	-13.84	40.20	A1367		
XMMU J114537.7+195330	54	-13.57	40.46	A1367		
XMMU J114507.7+195419	40	-13.54	40.50	A1367		
XMMU J114507.7+195757	39	-13.37	40.66	A1367		
XMMU J114508.4+194905	38	-13.57	40.46	A1367		
XMMU J114402.2+195700	153	-13.50	40.55	A1367	NGC 3842	0.021068
XMMU J114359.3+195632	59	-13.48	40.56	A1367	GALEXASC J114359.29+195633.6	0.023323
XMMU J140729.8-270104	128	-12.46	41.58	A3581	IC 4374	0.021798
XMMU J140714.2-270027	289	-13.63	40.45	A3581		
XMMU J140715.6-270932	1947	-12.89	41.24	A3581	ESO 510- G 066	0.024333
XMMU J140827.1-265828	106	-13.36	40.72	A3581		
XMMU J140656.6-265158	86	-13.79	40.29	A3581		
XMMU J140819.2-270150	109	-13.55	40.52	A3581		
XMMU J140751.8-265827	114	-13.97	40.11	A3581		
XMMU J140750.9-271138	130	-13.86	40.22	A3581		
XMMU J140701.2-265554	104	-13.87	40.21	A3581		
XMMU J140758.8-270425	91	-13.84	40.24	A3581		
XMMU J140751.4-271317	73	-13.63	40.45	A3581		
XMMU J140654.2-265314	56	-13.93	40.15	A3581		
XMMU J140737.0-270700	52	-13.99	40.09	A3581		
XMMU J140646.1-270112	69	-13.82	40.25	A3581		
XMMU J140743.0-265838	168	-14.00	40.08	A3581		
XMMU J140649.2-270031	51	-13.98	40.09	A3581		
XMMU J140720.9-265151	73	-13.58	40.49	A3581		
XMMU J140754.2-270555	118	-13.98	40.09	A3581		
XMMU J140805.5-270617	83	-13.78	40.30	A3581		
XMMU J140721.6-264716	134	-12.77	41.30	A3581		
XMMU J140720.6-270709	103	-13.68	40.39	A3581		
XMMU J140659.5-265213	58	-13.70	40.37	A3581		
XMMU J140803.6-270841	54	-13.49	40.58	A3581		
XMMU J140721.6-265328	50	-13.78	40.29	A3581		
XMMU J140643.9-265710	51	-13.87	40.20	A3581		
XMMU J140705.8-271047	71	-13.92	40.16	A3581		
XMMU J140811.5-265911	49	-13.83	40.24	A3581		
XMMU J140718.7-265415	97	-13.66	40.42	A3581		
XMMU J140825.4-270849	85	-13.25	40.82	A3581		
XMMU J140743.9-270648	102	-13.78	40.29	A3581		
XMMU J140759.8-271442	50	-13.29	40.78	A3581		
XMMU J140818.7-270533	46	-13.75	40.33	A3581		
XMMU J140801.4-271340	54	-13.68	40.39	A3581		
XMMU J140712.0-265007	51	-13.94	40.24	A3581	ESO 510- G 065	0.025671

Table B4. Properties of point sources studied in this work.

Object Name	Net Counts	Log Flux erg cm^{-2} s^{-1}	Log Luminosity erg s^{-1}	Cluster	Optical Counterpart	Redshift
XMMU J140840.1-270219	41	-13.74	40.33	A3581		
XMMU J140800.7-270542	55	-13.95	40.12	A3581		
XMMU J140844.4-270024	38	-13.62	40.46	A3581		
XMMU J140652.8-265631	186	-13.19	40.88	A3581		
XMMU J140806.5-270433	95	-13.67	40.41	A3581		
XMMU J140809.4-265902	81	-13.64	40.44	A3581		
XMMU J140752.1-264804	95	-13.08	40.99	A3581		
XMMU J140757.1-265318	36	-13.40	40.67	A3581		
XMMU J140741.5-265121	54	-13.41	40.66	A3581		
XMMU J140650.2-270206	49	-13.94	40.14	A3581		
XMMU J140645.6-265433	39	-13.63	40.44	A3581		
XMMU J140750.9-270622	49	-13.92	40.15	A3581		
XMMU J140632.6-270045	43	-13.88	40.20	A3581		
XMMU J152305.3+083631	1237	-12.71	41.72	A2063	CGCG 077-097	0.034174
XMMU J152252.6+083735	102	-12.95	41.49	A2063		
XMMU J152318.7+084319	67	-13.73	40.72	A2063		
XMMU J152342.5+084535	64	-13.22	41.23	A2063		
XMMU J152249.9+083643	201	-13.28	41.16	A2063		
XMMU J152323.5+083212	107	-13.47	40.97	A2063		
XMMU J152331.2+082744	42	-13.86	40.59	A2063		
XMMU J152326.9+083428	265	-13.34	41.11	A2063		
XMMU J152250.9+084447	34	-13.21	41.21	A2063		
XMMU J152256.6+083858	38	-13.59	40.86	A2063	2MASX J15225650+0839004	0.03361
XMMU J152237.4+083530	42	-13.59	40.85	A2063		
XMMU J152248.0+082759	87	-13.61	40.84	A2063		
XMMU J152226.9+083556	35	-13.93	40.52	A2063		
XMMU J152322.3+082159	46	-13.22	41.23	A2063		
XMMU J152248.0+084306	44	-13.94	40.51	A2063		
XMMU J152359.5+084117	32	-13.55	40.90	A2063		
XMMU J152404.6+084115	31	-13.59	40.86	A2063		
XMMU J152312.5+083259	1820	-12.10	42.40	A2063	2MASX J15231224+0832590	0.036619
XMMU J152327.1+083553	53	-13.22	41.27	A2063		
XMMU J152240.6+082621	47	-13.28	41.20	A2063		
XMMU J152234.3+082854	31	-13.94	40.55	A2063		
XMMU J152225.9+084134	30	-13.92	40.57	A2063		
XMMU J152219.7+083803	94	-13.59	40.90	A2063		
XMMU J152224.7+084244	33	-13.66	40.82	A2063		
XMMU J113449.4+490438	357	-13.73	40.68	A1314	IC 712	0.03335
XMMU J113450.2+490326	344	-13.76	40.65	A1314		
XMMU J113439.1+490623	53	-13.95	40.46	A1314		
XMMU J113409.1+491516	48	-12.22	42.28	A1314	2MASX J11340896+4915162	0.03723
XMMU J113543.9+490215	273	-12.13	42.15	A1314	MCG+08-21-065	0.02967
XMMU J113421.6+490050	334	-13.47	40.95	A1314		
XMMU J113446.6+485721	200	-13.64	40.72	A1314	IC 711	0.03160
XMMU J113447.3+490133	301	-13.73	40.69	A1314		
XMMU J113359.3+490343	298	-13.27	41.09	A1314	IC 708	0.03165
XMMU J113408.4+490318	207	-13.16	41.24	A1314		
XMMU J113425.0+490647	111	-13.50	40.90	A1314		
XMMU J113359.5+491246	69	-13.76	40.65	A1314	LEDA 97398	0.031600
XMMU J113509.1+490658	91	-13.88	40.54	A1314		
XMMU J113441.8+490918	118	-13.86	40.56	A1314		
XMMU J113451.4+491203	137	-13.56	42.36	A1314		
XMMU J113548.5+491150	49	-13.48	40.93	A1314		
XMMU J113355.9+490955	61	-13.32	41.08	A1314		
XMMU J113424.7+491230	38	-13.85	40.55	A1314		
XMMU J113425.9+490909	81	-13.83	40.59	A1314		
XMMU J113431.4+485354	34	-13.91	40.50	A1314		
XMMU J113454.2+485506	30	-13.87	40.53	A1314		
XMMU J113404.6+485519	76	-13.38	41.02	A1314		
XMMU J113331.2+485920	66	-13.85	40.57	A1314		
XMMU J113412.2+485614	38	-13.99	40.41	A1314		
XMMU J113420.9+490937	47	-13.89	40.52	A1314		
XMMU J113424.7+491623	31	-13.76	40.65	A1314		
XMMU J113526.2+485555	30	-13.77	40.62	A1314		
XMMU J113533.8+485620	34	-13.94	40.47	A1314		
XMMU J113317.3+490607	79	-13.19	41.22	A1314		

Table B5. Properties of point sources studied in this work.

Object Name	Net Counts	Log Flux erg cm^{-2} s^{-1}	Log Luminosity erg s^{-1}	Cluster	Optical Counterpart	Redshift
XMMU J113328.3+491218	48	-13.66	40.75	A1314		
XMMU J113517.8+491259	40	-13.82	40.59	A1314		
XMMU J113334.6+485659	35	-13.86	40.55	A1314		
XMMU J113347.3+490614	37	-13.96	40.45	A1314		
XMMU J113330.0+490901	31	-13.77	40.63	A1314		
XMMU J113423.0+490326	42	-13.43	40.97	A1314		
XMMU J113408.6+485932	39	-13.01	41.39	A1314		
XMMU J113406.5+490622	30	-13.55	40.85	A1314		
XMMU J113539.8+485459	143	-13.05	41.36	A1314		
XMMU J113554.7+485809	31	-13.16	41.26	A1314		
XMMU J140141.8-113625	589	-13.20	41.31	A1836	MCG -02-36-002	0.037776
XMMU J140139.4-113749	197	-13.37	41.11	A1836		
XMMU J140147.8-113438	31	-13.65	40.81	A1836		
XMMU J140131.4-113309	37	-13.81	40.66	A1836		
XMMU J140215.6-113748	417	-12.63	41.84	A1836		
XMMU J140207.9-113553	411	-13.42	41.06	A1836		
XMMU J140210.1-114131	164	-13.90	40.59	A1836		
XMMU J140143.0-113059	85	-13.23	41.23	A1836		
XMMU J140207.2-114351	62	-13.75	40.73	A1836		
XMMU J140157.8-113927	71	-13.21	41.06	A1836		
XMMU J140145.4-113133	66	-13.64	40.84	A1836		
XMMU J140123.0-114535	29	-13.94	40.54	A1836		
XMMU J140131.9-113925	31	-13.46	41.12	A1836	2MASX J14013206-1139261	0.041662
XMMU J140124.5-112832	30	-13.81	40.67	A1836		
XMMU J140200.2-112752	94	-13.64	40.84	A1836		
XMMU J140142.5-112754	84	-13.63	40.86	A1836		
XMMU J140155.9-112952	101	-13.81	40.67	A1836		
XMMU J140135.5-112708	32	-13.39	41.05	A1836		
XMMU J140212.5-114443	33	-13.58	40.88	A1836		
XMMU J140125.4-114717	39	-13.51	40.96	A1836		
XMMU J140057.7-113746	32	-13.46	41.00	A1836		
XMMU J140102.0-113316	69	-13.46	41.12	A1836		
XMMU J140107.7-112915	34	-13.44	41.14	A1836		
XMMU J140042.4-113447	39	-13.03	41.56	A1836		
XMMU J140043.8-113731	38	-13.42	41.18	A1836		
XMMU J140149.0-113837	501	-12.91	41.70	A1836		
XMMU J140201.7-113408	51	-13.56	41.03	A1836		
XMMU J140155.7-113808	54	-13.91	40.59	A1836	2MASX J14015570-1138043	0.036979
XMMU J140057.6-114051	49	-13.68	40.82	A1836		
XMMU J140230.7-113646	42	-13.80	40.70	A1836		
XMMU J140217.3-112612	29	-13.91	40.59	A1836		
XMMU J140130.5-112247	37	-13.72	40.78	A1836		
XMMU J011146.5-613139	445	-13.92	40.29	AS137	NGC 0432	0.026929
XMMU J011142.8-613106	448	-13.64	40.56	AS137		
XMMU J011205.4-613255	328	-13.47	40.73	AS137		
XMMU J011208.8-613214	238	-13.68	40.52	AS137		
XMMU J011150.0-613348	103	-13.89	40.30	AS137		
XMMU J011134.8-613414	88	-13.92	40.27	AS137		
XMMU J011142.1-612649	641	-13.19	41.01	AS137		
XMMU J011211.4-612126	188	-13.71	40.49	AS137		
XMMU J011014.3-613852	177	-12.91	41.29	AS137		
XMMU J011120.3-612958	159	-13.70	40.50	AS137		
XMMU J011222.9-612811	104	-13.81	40.39	AS137		
XMMU J011116.1-612822	122	-13.98	40.21	AS137		
XMMU J011123.1-612054	83	-13.34	40.85	AS137		
XMMU J011127.4-612612	104	-13.49	40.70	AS137		
XMMU J011210.5-612807	110	-13.99	40.21	AS137		
XMMU J011207.4-614033	99	-13.95	40.25	AS137		
XMMU J011109.0-613049	81	-13.49	40.70	AS137		
XMMU J011115.6-613242	111	-13.65	40.55	AS137		
XMMU J011211.3-612439	92	-13.53	40.66	AS137		
XMMU J011128.8-613519	94	-13.71	40.48	AS137		
XMMU J011154.6-614035	62	-13.73	40.46	AS137		
XMMU J011136.7-612338	79	-13.90	40.29	AS137		
XMMU J011144.0-614135	38	-13.79	40.40	AS137		
XMMU J011325.0-612746	67	-13.99	40.21	AS137		
XMMU J011201.8-612157	55	-13.89	40.30	AS137		

Table B6. Properties of point sources studied in this work.

Object Name	Net Counts	Log Flux erg cm^{-2} s^{-1}	Log Luminosity erg s^{-1}	Cluster	Optical Counterpart	Redshift
XMMU J011105.5-612548	141	-13.02	41.16	AS137		
XMMU J010949.4-613153	174	-13.06	41.13	AS137		
XMMU J011220.2-613752	83	-13.57	40.62	AS137		
XMMU J011059.5-613832	52	-13.94	40.25	AS137		
XMMU J011114.5-612922	48	-13.78	40.41	AS137		
XMMU J011251.4-613959	65	-13.77	40.43	AS137	2MASX J01125179-6139513	0.026442
XMMU J011058.3-612752	107	-13.48	40.71	AS137		
XMMU J011318.7-613133	64	-13.33	40.86	AS137		
XMMU J011022.1-613043	46	-13.70	40.49	AS137		
XMMU J011234.0-613615	29	-13.73	40.46	AS137		
XMMU J011054.8-612940	42	-13.83	40.36	AS137		
XMMU J011315.5-613609	47	-13.67	40.52	AS137		
XMMU J011029.9-612637	37	-13.92	40.27	AS137		
XMMU J011244.1-612341	30	-13.71	40.48	AS137		
XMMU J011255.6-613655	31	-13.62	40.57	AS137		
XMMU J011249.7-612938	39	-13.89	40.30	AS137		
XMMU J011340.9-613101	38	-13.49	40.70	AS137		
XMMU J011247.9-613645	35	-13.95	40.25	AS137		
XMMU J011157.1-613920	31	-13.89	40.30	AS137		
XMMU J011048.5-614303	30	-13.72	40.48	AS137		
XMMU J011202.3-613006	93	-13.47	40.72	AS137		
XMMU J011142.8-612813	85	-13.69	40.51	AS137		
XMMU J011213.1-612015	81	-13.36	40.84	AS137		
XMMU J011314.2-612331	65	-13.41	40.78	AS137		
XMMU J011231.9-611906	37	-13.55	40.64	AS137		
XMMU J011220.4-613648	50	-13.65	40.55	AS137		
XMMU J011314.3-612249	37	-13.46	40.73	AS137		
XMMU J010959.0-612601	28	-13.46	40.73	AS137		
XMMU J011007.3-612417	30	-13.71	40.49	AS137		
XMMU J141220.9-342022	1460	-13.83	40.72	AS758	MCG-06-31-029	0.03850
XMMU J141117.5-341116	302	-13.09	41.42	AS758		
XMMU J141216.6-342422	988	-13.06	41.46	AS758		
XMMU J141226.2-341715	746	-13.49	41.03	AS758		
XMMU J141201.2-341548	430	-13.50	41.03	AS758		
XMMU J141308.6-342105	197	-13.01	41.49	AS758		
XMMU J141200.2-341657	272	-13.85	40.68	AS758		
XMMU J141157.6-341840	303	-13.92	40.61	AS758		
XMMU J141231.7-342141	363	-13.79	40.74	AS758		
XMMU J141124.7-342353	248	-13.59	40.94	AS758		
XMMU J141253.8-342638	243	-13.85	40.68	AS758		
XMMU J141312.2-342051	123	-13.69	40.83	AS758		
XMMU J141200.0-342245	115	-13.91	40.61	AS758		
XMMU J141216.8-342556	112	-13.98	40.54	AS758		
XMMU J141246.8-342532	139	-13.80	40.72	AS758		
XMMU J141145.6-342441	177	-13.89	40.64	AS758		
XMMU J141200.7-341036	123	-13.67	40.85	AS758		
XMMU J141311.3-342216	281	-13.69	40.84	AS758		
XMMU J141229.3-341741	149	-13.96	40.67	AS758	2MASX J14122917-3417417	0.04300
XMMU J141134.3-342353	71	-13.89	40.63	AS758		
XMMU J141210.3-343142	64	-13.31	41.20	AS758		
XMMU J141259.5-341734	93	-13.79	40.72	AS758		
XMMU J141241.3-342659	135	-13.80	40.72	AS758		
XMMU J141149.9-343008	102	-13.90	40.63	AS758		
XMMU J141127.8-342255	66	-13.81	40.71	AS758		
XMMU J141246.3-342816	63	-13.71	40.80	AS758		
XMMU J141314.2-341952	88	-13.62	40.89	AS758		
XMMU J141215.8-342717	30	-13.74	40.77	AS758		
XMMU J141249.7-342552	62	-13.82	40.69	AS758		
XMMU J141120.2-341449	63	-13.55	40.96	AS758		
XMMU J141207.7-340830	67	-13.88	40.64	AS758		
XMMU J141232.8-341653	70	-13.97	40.54	AS758		
XMMU J141118.2-342059	35	-13.68	40.82	AS758		
XMMU J141230.7-340947	757	-13.56	40.98	AS758		
XMMU J141255.7-341247	362	-13.78	40.75	AS758		
XMMU J141216.6-341034	179	-13.50	41.01	AS758		
XMMU J141301.7-341331	63	-13.85	40.67	AS758		
XMMU J141241.6-341103	119	-13.90	40.62	AS758		

Table B7. Properties of point sources studied in this work.

Object Name	Net Counts	Log Flux erg cm^{-2} s^{-1}	Log Luminosity erg s^{-1}	Cluster	Optical Counterpart	Redshift
XMMU J141146.6-341906	87	-13.86	40.65	AS758		
XMMU J141219.9-342557	89	-13.86	40.65	AS758		
XMMU J141144.2-341353	74	-13.88	40.63	AS758		
XMMU J141209.8-341327	55	-13.71	40.80	AS758		
XMMU J141139.1-340615	79	-13.50	41.02	AS758		
XMMU J141117.0-342710	74	-13.68	40.84	AS758		
XMMU J141204.1-340538	42	-13.37	41.13	AS758		
XMMU J141221.6-342716	52	-13.96	40.56	AS758		
XMMU J141139.6-340810	72	-13.77	40.75	AS758		
XMMU J141141.0-340707	39	-13.77	40.75	AS758		
XMMU J141137.0-340736	38	-13.36	41.15	AS758		
XMMU J141236.7-342930	54	-13.95	40.57	AS758		
XMMU J141302.4-342438	37	-13.86	40.64	AS758		
XMMU J141311.8-341709	40	-13.75	40.76	AS758		
XMMU J141234.3-341849	151	-13.58	40.93	AS758		
XMMU J141240.1-341617	56	-13.64	40.88	AS758		
XMMU J141245.4-342343	343	-13.35	41.18	AS758		
XMMU J141304.3-342557	43	-13.44	41.07	AS758		
XMMU J141215.6-341628	42	-13.98	40.54	AS758		
XMMU J141149.9-341643	46	-13.95	40.57	AS758		
XMMU J141300.2-342947	29	-13.91	40.61	AS758		
XMMU J141223.0-341330	218	-13.47	41.06	AS758		
XMMU J231638.6-022527	522	-12.54	41.67	RXCJ2315.7-0222		
XMMU J231544.4-022254	1768	-13.61	40.56	RXCJ2315.7-0222	NGC 7556	0.025041
XMMU J231624.5-021457	310	-13.35	40.80	RXCJ2315.7-0222		
XMMU J231553.8-022615	235	-13.78	40.38	RXCJ2315.7-0222		
XMMU J231623.8-022550	132	-13.54	40.61	RXCJ2315.7-0222		
XMMU J231523.5-021660	130	-13.67	40.48	RXCJ2315.7-0222		
XMMU J231637.4-021950	110	-13.83	40.32	RXCJ2315.7-0222	NGC 7566	0.026548
XMMU J231535.8-021727	71	-13.99	40.16	RXCJ2315.7-0222		
XMMU J231555.9-021644	85	-13.33	40.81	RXCJ2315.7-0222		
XMMU J231610.3-021128	74	-13.80	40.35	RXCJ2315.7-0222		
XMMU J231605.0-022533	59	-13.95	40.20	RXCJ2315.7-0222		
XMMU J231527.6-021525	60	-13.56	40.58	RXCJ2315.7-0222		
XMMU J231618.2-021330	37	-13.58	40.57	RXCJ2315.7-0222		
XMMU J231610.3-021502	29	-13.47	40.67	RXCJ2315.7-0222		
XMMU J231610.3-021238	36	-13.76	40.39	RXCJ2315.7-0222		
XMMU J231600.0-022943	159	-13.23	40.91	RXCJ2315.7-0222		
XMMU J231619.7-021351	50	-13.62	40.53	RXCJ2315.7-0222		
XMMU J231552.3-023008	73	-13.76	40.39	RXCJ2315.7-0222		
XMMU J231547.8-022841	86	-13.94	40.21	RXCJ2315.7-0222		
XMMU J231631.4-021247	471	-12.88	41.33	RXCJ2315.7-0222		
XMMU J231642.2-022452	114	-12.87	41.26	RXCJ2315.7-0222		
XMMU J231504.6-022254	59	-13.62	40.53	RXCJ2315.7-0222		
XMMU J231559.0-021042	31	-13.69	40.46	RXCJ2315.7-0222		
XMMU J231614.4-021426	45	-13.97	40.18	RXCJ2315.7-0222		
XMMU J231544.6-023059	44	-13.82	40.32	RXCJ2315.7-0222		
XMMU J231538.9-021608	37	-13.60	40.54	RXCJ2315.7-0222		
XMMU J231633.8-023017	35	-13.67	40.48	RXCJ2315.7-0222		
XMMU J231500.7-022515	91	-13.36	40.85	RXCJ2315.7-0222		
XMMU J231602.2-022532	47	-13.83	40.38	RXCJ2315.7-0222		
XMMU J231513.7-022235	31	-13.74	40.46	RXCJ2315.7-0222		
XMMU J231527.1-022812	38	-13.65	40.55	RXCJ2315.7-0222		
XMMU J231610.3-023034	29	-13.58	40.62	RXCJ2315.7-0222		
XMMU J231547.8-023050	45	-13.95	40.26	RXCJ2315.7-0222		
XMMU J231556.6-022415	30	-13.54	40.65	RXCJ2315.7-0222		

This paper has been typeset from a TeX/LaTeX file prepared by the author.